IOP Publishing Plasma Physics and Controlled Fusion

Plasma Phys. Control. Fusion **00** (2019) 000000 (10pp)

Probing thermal Weibel instability in optical-field-ionized plasmas using relativistic electron bunches

Chaojie Zhang, Chen-Kang Huang, Ken A Marsh and Chan Joshi

Department of Electrical and Computer Engineering, University of California Los Angeles, Los Angeles, CA 90095, United States of America

E-mail: chaojiez@ucla.edu

Received 2 July 2019, revised 6 November 2019
Accepted for publication 13 December 2019
Published DD MM 2020

Abstract

Thermal Weibel instability driven by anisotropic velocity distributions is an important mechanism for self-generating magnetic fields in both laboratory and space plasmas. However, there is a lack of experimental data on thermal Weibel instability due to the difficulty of initializing anisotropic distributions in a controllable manner as well as the challenge of probing the magnetic fields with high spatiotemporal resolution. Here we show that the initial electron velocity distribution of optical-field-ionized plasmas can be easily manipulated by changing laser polarization and such plasmas are unstable to the thermal Weibel instability. The topology of the self-generated magnetic fields depends on the laser polarization. We propose to use ultrashort relativistic electron beams such as those produced by a laser wakefield accelerator as a probe to record the spatiotemporal evolution of the magnetic fields. By taking a series of snapshots of the magnetic fields at different times, the wavevector spectrum and growth rate of the instability can be deduced and compared with kinetic theory.

Keywords: Weibel instability, optical field ionization, kinetic plasma instability, electron probe, magnetic fields

SQ1 (Some figures may appear in colour only in the online journal)

1. Introduction

Thermal Weibel instability is a kinetic instability that grows in plasmas with anisotropic velocity distributions and leads to self-generation of magnetic fields. It has been extensively studied in both theory and simulations since it had been proposed [1] due to its role in basic plasma physics and its possible presence in many physical phenomena such as collisionless shocks [2–5], gamma-ray bursts [6, 7], and magnetic fields generation in galactic and interstellar plasmas [8–10].

Weibel instability is closely related to current filamentation instability (CFI) which is driven by interpenetrating streams of plasmas. The interpenetrating streams can be seen as one limit of anisotropic distributions [11]. Because of this similarity, the term 'Weibel instability' and 'filamentation instability' have often been used interchangeably in the literature. However, there are differences between these two instabilities [12]. For instance, in the linear phase and without including ion motion, Weibel instability is purely transverse thus has no electrostatic component [1]. The CFI, however, is not purely transverse unless the counter-propagating currents are symmetric so that they can pinch at the same rates [13]. The CFI may also coincides with the presence of two-stream instability to generate the so-called oblique mode [12, 14]. In this paper we differentiate these two instabilities and use the term 'thermal Weibel instability' [15] to refer to the instability driven by anisotropic velocity distributions as proposed by Weibel [1].

CFI has been experimentally studied by either passing a relativistic electron beam through a plasma [16–21] or by creating two interpenetrating plasmas [2, 4, 22, 23]. In the former case, the system is dominated by electron CFI whereas in the latter case, the system is dominated by ion CFI.

Recently, electron CFI was also observed in dense plasmas ablated from laser-irradiated solid targets using Faraday rotation effect [24]. However, to the best of our knowledge, there is no experimental verification on thermal Weibel instability to date, despite of the voluminous theoretical and simulation work on this topic [1, 12, 25–27]. It remains a challenging problem due to the difficulty of initializing known anisotropic distribution(s) on one hand and the challenge of directly measuring the magnetic field structures that evolve in the plasma with high spatiotemporal resolution on the other hand.

In this paper, we present simulation results which show that anisotropic plasmas initialized by optical-field-ionization (OFI) using either a circularly or a linearly polarized laser are unstable to thermal Weibel instability and that it is possible to measure the spatiotemporal evolution of the self-generated magnetic fields using an ultrashort relativistic electron beam as a probe. We show that the self-generated magnetic fields form different topological structures when plasmas are initialized by lasers with different (circular or linear) polarizations. By taking snapshots of the magnetic fields at different times, the linear growth of the thermal Weibel instability can be recorded. From these snapshots we can deduce the evolution of wavevector spectrum and growth rate of the instability and compare these with predictions of the kinetic theory.

2. Self-generation of magnetic fields in OFI plasmas

2.1. Kinetic theory of thermal Weibel instability

Assume a plasma with the electron velocity distribution (EVD) function of $f(v) = \frac{n_0}{(2\pi)^{3/2} vth_x vth_y vth_z} \exp\left[-\left(\frac{v_x^2}{2vth_x^2} + \frac{v_y^2}{2vth_y^2} + \frac{v_z^2}{2vth_z^2}\right)\right]$ and $vth_x = vth_y > vth_z$. The anisotropy is then defined as $A \equiv \frac{T_{hot}}{T_{cold}} - 1 = \frac{vth_{x,y}^2}{vth_z^2} - 1$. The linear stability analysis gives the dispersion relation of the plasma as $k_z^2 c^2 - \omega^2 - \omega_p^2\left(A + (A+1)\frac{\omega}{\sqrt{2} k_z vth_z} Z\left(\frac{\omega}{\sqrt{2} k_z vth_z}\right)\right) = 0$, where $\omega_p = \sqrt{4\pi n_0 e^2/m_e}$ is the plasma frequency and $Z(\zeta) = \pi^{-1/2}\int_{\infty}^{-\infty} \frac{e^{-t^2}}{t-\zeta} dt$ is the plasma dispersion function. Here we have assumed that the wave vector is in z direction and the $\boldsymbol{B}$ field is in the x–y plane. By solving the dispersion relation, one can find the growth rate of thermal Weibel instability $\gamma = i\omega$ for unstable modes with wavevectors within the range of $0 < \frac{k_z c}{\omega_p} < \sqrt{A}$ for any arbitrary $A > 0$. The wavevector of the unstable mode is predominantly along the low-temperature direction, i.e. $\boldsymbol{k} \approx \hat{z} k_z$. Thermal Weibel instability is transverse, therefore the magnetic field is predominantly along the transverse directions, namely $\boldsymbol{B} \approx \hat{x} B_x + \hat{y} B_y$ and $|B_x| \approx |B_y| \gg |B_z|$. As we will show later this corresponds to the case where the plasma is ionized by a circularly polarized laser propagating along z direction. On the other hand, if the plasma is hot in one direction and cold in the other two orthogonal directions, for instance, $vth_x > vth_y = vth_z$, the wavevector of the unstable mode will be $\boldsymbol{k} \approx \hat{y} k_y + \hat{z} k_z$ and the magnetic field is $\boldsymbol{B} \approx \hat{y} B_y + \hat{z} B_z$ with $\boldsymbol{k} \cdot \boldsymbol{B} = k_y B_y + k_z B_z = 0$. This corresponds to the case where the plasma is ionized by a linearly polarized laser which polarizes along x direction and propagates along z direction.

2.2. Anisotropic temperature plasma initialized by optical-field ionization

An intense, infrared (IR) laser pulse can ionize atoms rapidly in the tunneling regime during its rising edge. Once being released from the parent ion, electrons start oscillating in the electromagnetic field of the laser. When the laser is gone, the electrons are left with a residual velocity (momentum) that depends on the phase when the electrons are ionized and the polarization of the laser. This process thus enables one to control the initial EVD of the plasma and can be self-consistently modeled in particle-in-cell (PIC) simulations. In this section, we present results of 3D simulations using the OSIRIS [28] code to show the initialization of anisotropic EVD of OFI plasmas. In these simulations, the ADK [29] ionization model is used but we should point out that because we consider a scenario where the laser is intense enough to rapidly fully ionize helium, different ionization models give the same results.

As shown in figure 1(a), if the laser is circularly polarized, the electric field of the laser rotates in the plane perpendicular to the propagation direction with an almost constant amplitude (within each laser cycle). Therefore, the residual velocity of the electrons resembles a cylindrical distribution in the transverse velocity space. The plasma is cold in the laser propagation direction but hot in the transverse plane. Because of the different ionization potentials of the two electrons of helium, the velocity distribution consists of two distinct rings with the radius of the ring being proportional to the ionization potential. Such an anisotropic distribution initialized by a circularly polarized laser has been confirmed in recent experiments [30].

Along any particular direction in the transverse plane, such a velocity distribution can be seen as consisting of four quasi-Gaussian streams, thus the plasma is unstable to both streaming and filamentation instabilities. The density fluctuations associated with these instabilities have been observed in experiments using Thomson scattering of a femtosecond probe laser [31]. The electric fields associated with the streaming instability accelerate cold (He^{1+}) electrons and decelerate hot (He^{2+}) electrons therefore cause collisionless relaxation of the distribution in the transverse plane. The filamentation instability self-generates magnetic fields which isotropize the plasma. The streaming instability has a growth rate of $\gamma \sim 0.1\omega_p$, therefore the plasma relaxes very rapidly in tens of plasma periods. Figure 1(b) shows the velocity distribution 1 ps after the plasma being created. Clearly, the ring structure has disappeared and the temperature in the laser propagation direction has increased significantly. At this time, the distribution can be approximated by Maxwellian

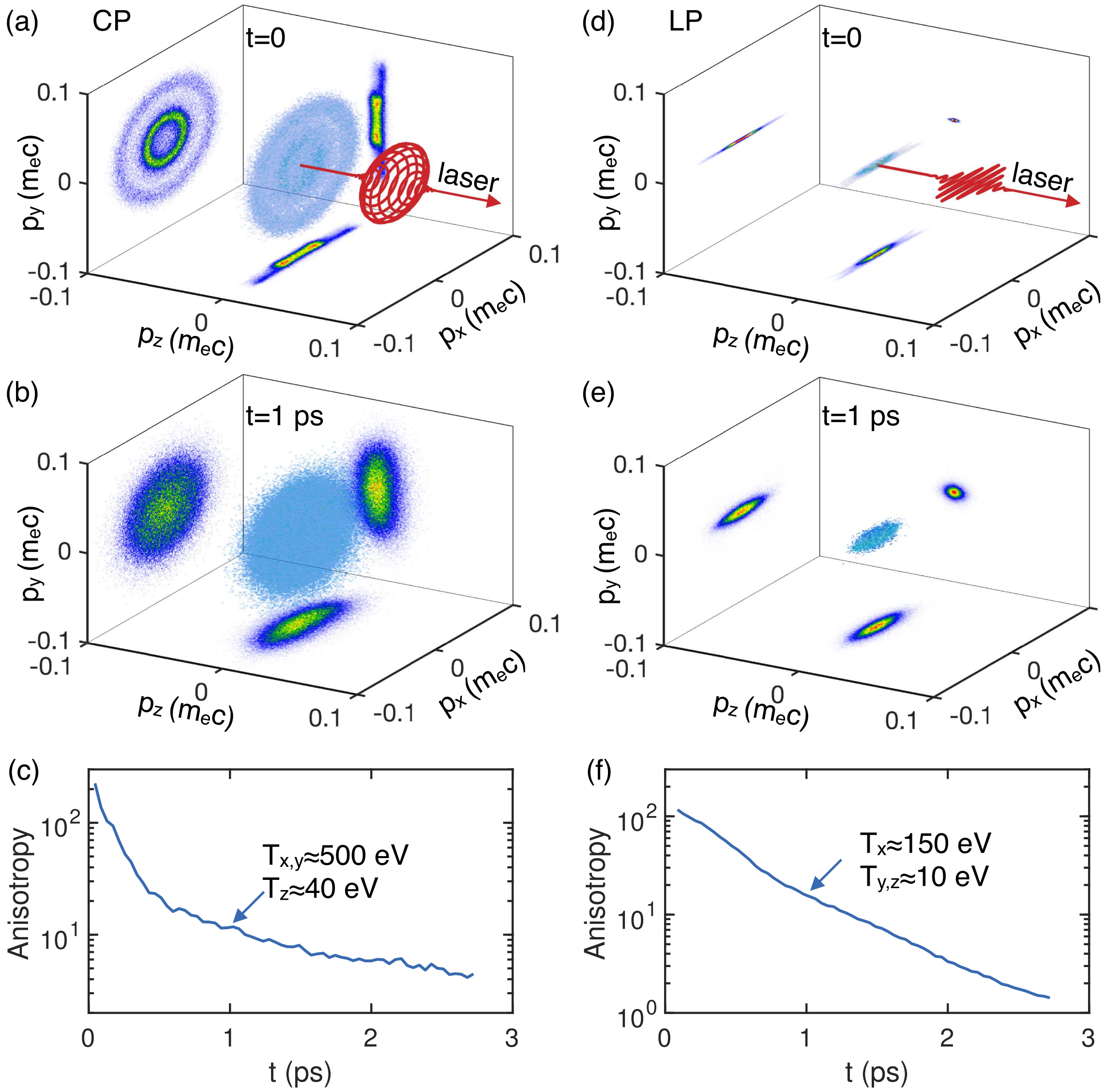

Figure 1. Anisotropic plasma initialized by optical-field-ionization. (a) shows the initial EVD of helium electrons ionized by a circularly polarized laser and (b) shows the EVD at 1 ps after the initialization. The dimensions of the 3D simulation box are chosen as $1000 \times 500 \times 500\ c/\omega_0$, divided into $1500 \times 300 \times 300$ cells along the z, x and y direction, respectively. In each cell, 64 particles are initialized. The density of the uniform helium gas is 5×10^{18} cm^{-3}. A laser with pulse duration $\tau = 60$ fs, spot size $w_0 = 8\ \mu$m and normalized vector potential $a_0 = 0.2$ is launched from the left wall and focused to the right edge of the simulation box. The electrons within a $\Delta z = 5\ \mu$m slab at the center of the simulation box are used to generate the distributions. The evolution of the anisotropy of the plasma is shown in (c). (d)–(f) show the corresponding results for a linearly polarized laser.

distributions in all directions with $T_{x,y} \approx 500$ eV and $T_z \approx 40$ eV. The anisotropy of the plasma is therefore $A \equiv \frac{T_{hot}}{T_{cold}} - 1 = 11.5$. The evolution of the anisotropy of the plasma is shown in figure 1(c). The initial anisotropy when the laser has just passed is more than 100, indicating that the plasma is highly anisotropic (see figure 1(a)). Then it keeps dropping due to the isotropization of the plasma driven by kinetic instabilities. It is worth noting that the initial EVD is independent of plasma density provided that the density is not too high to substantially deplete the laser energy during ionization. However, the anisotropy may drop more rapidly for higher densities due to larger instability growth and e–e collision rates.

As we have explained, initial EVD of OFI plasmas can be manipulated by changing laser polarization. Figure 1(d) shows the initial EVD of a plasma ionized by a linearly polarized laser. In this case, the plasma is hot in the laser polarization direction but cold in the other two orthogonal directions. Although not as clear as in the circular polarization case due to the overlapping of the two groups (He^{1+} and He^{2+}) of electrons in the velocity space, there are also some subtle structures in the distribution (see the projection on the x–z plane) due to the different ionization potentials of the two electrons of helium. In the laser polarization direction the initial distribution can be well approximated by two Maxwellian distributions with different temperatures, as have been confirmed in experiments [30]. Similar to the CP case, after 1 ps, the distribution can be approximated by Maxwellian

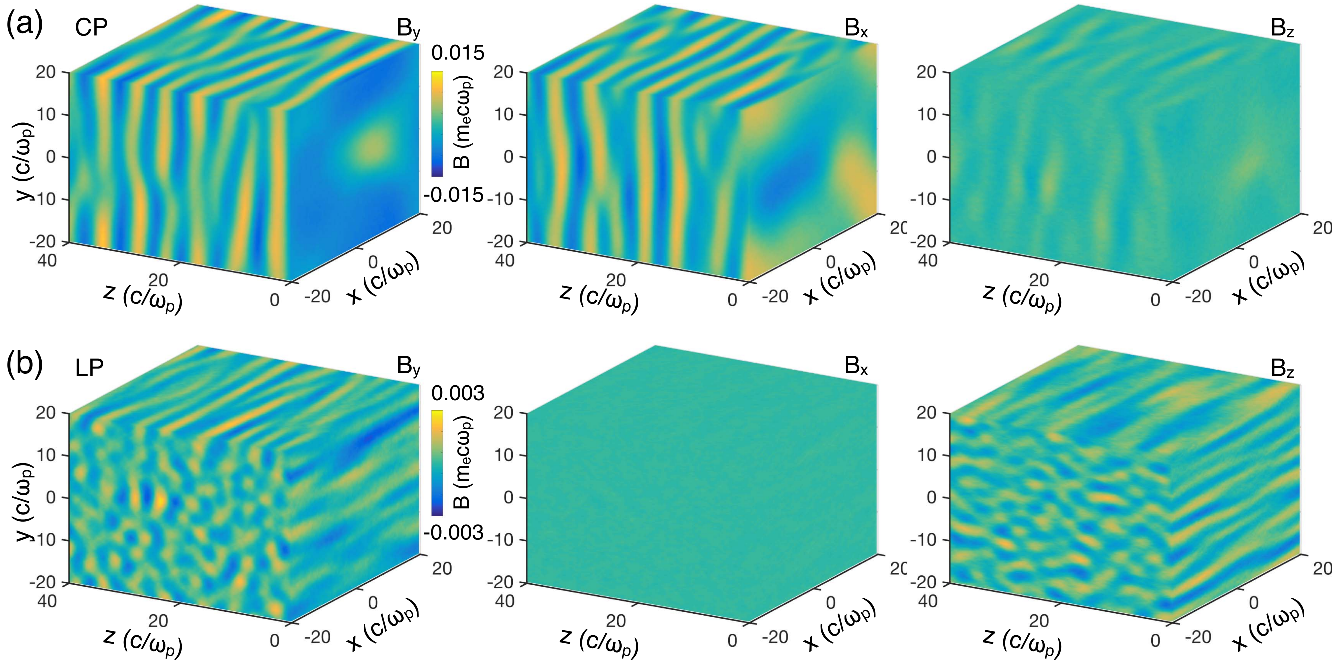

Figure 2. Different topological structures of self-generated magnetic fields. (a) and (b) show the Cartesian components of the magnetic fields in plasmas with initial EVDs corresponding to the CP and LP cases, respectively. In each subplot, the colour bar applies to all three components. The magnitude of B_x fields in (b) is so small that is invisible.

distributions in all three directions with $T_x \approx 150$ eV and $T_{y,z} \approx 10$ eV, respectively. We note that these temperatures may be slightly different due to numerical effects if the resolution (cell size) of the simulation changes. Nevertheless, this subtlety does not affect the analysis and results shown below.

The main takeaway from the above discussion is that even though the initial anisotropy following ionization is extremely large in both the CP and LP cases, the plasma has an anisotropy of $\sim$10 after just $\sim$1 ps which drives the thermal Weibel instability. Although the anisotropy is similar, the temperature tensor is quite different in these two cases. In the CP case, the plasma is hot in the two transverse directions but cold in the laser propagation direction; whereas in the LP case, the plasma is hot in the laser polarization direction but cold in the other two orthogonal directions. Such different temperature tensors will lead to self-generation of magnetic fields with different topological structures, as we shall see in the next section.

2.3. Topological structure of self-generated magnetic fields

To model thermal Weibel instability driven by anisotropic distributions accurately with available computation resources, we performed 3D simulations using pre-ionized plasmas with the temperatures obtained from the aforementioned simulations. For the CP case, we set $T_{x,y} = 500$ eV and $T_z = 40$ eV. The plasma density is $n_p = 5 \times 10^{18}$ cm^{-3}. The dimensions of the simulation box are 120, 40 and 40 c/ω_p in the z, x and y direction, respectively. The cell size is 0.2 c/ω_p in all three directions. In each cell, 64 particles with quadratic shape are initialized. Uniform density plasma with fixed ion background is used. Periodic boundary conditions for both the fields and the particles are used in all directions.

Figures 2(a) and (b) show the topological structures of the Cartesian components of the magnetic fields for the CP and LP case, respectively. The snapshots are taken at $t = 100\,T_p$ where $T_p = 2\pi/\omega_p$ is the plasma period. For $n_e = 5 \times 10^{18}$ cm^{-3}, this corresponds to 5 ps. For the CP case, because the plasma is cold in z direction, the magnetic fields self-organize themselves into a quasi-static structure with the wavevector predominantly along z direction. On the contrary, in the LP case, the magnetic fields resemble to a quasi-static structure with wavevectors randomly distributed in the y–z plane. In the CP case, B_x field has similar structures as B_y field and B_z field is much smaller compared with $B_{x,y}$. In the LP case, B_z has similar structures as B_y field and B_x field is much smaller than $B_{y,z}$.

The reason for the difference in the topological structures in the two polarization cases is as follows. In an anisotropic plasma, the counter-propagating microscopic currents repel each other whereas the co-propagating microscopic currents attract each other, which generates macroscopic current filaments and keeps amplifying the magnetic field. As a result, the plasma breaks into current filaments primarily in the cold temperature direction. In the CP case, the plasma is cold in z direction therefore the plasma breaks into current sheets in that direction. The associated magnetic fields thus have a wavevector predominantly along z direction as can be seen in figure 2(a). In the LP case, because the plasma is cold in both y and z directions, the plasma breaks into current filaments in both directions. Therefore, the magnetic fields have wavevectors randomly distributed in the y–z plane.

3. Probing Weibel instability using ultrashort electron beams

As mentioned in the introduction section, direct measurements of magnetic fields associated with the thermal Weibel instability are challenging. One commonly used diagnostic for probing magnetic field is to measure the rotation of polarization of a probe laser induced by the Faraday effect [17, 24, 32]. This method can achieve femtosecond temporal resolution but is more suitable for measuring mega-Gauss level magnetic fields that lead to a measurable rotation angle of the polarization. Proton radiography has also been used to capture the magnetic field structures associated with CFI [4, 22, 23] but with a typical temporal resolution of $\gg$1 ps.

To achieve both high spatiotemporal resolution and high sensitivity to Tesla-level magnetic fields generated by thermal Weibel instability in OFI plasmas, here we propose to use ultrashort relativistic electron beams as a probe. Similar to proton radiography, electrons will be deflected by the magnetic fields as they traverse through the plasma therefore to form density structures after propagating in vacuum for an optimum distance. The modulated density profile of the probe beam then reflects the magnetic field distributions in the plasma. An electron beam with a moderate energy of tens of MeV is suitable for measuring the magnetic fields in OFI plasmas with an integrated magnitude on the order of $B \cdot W \approx 100\, T \cdot \mu$m, here W is the width of the plasma. The measurable quantity is the modulation of the density profile of the electron beam, the magnitude of which increases linearly as the drift distance after the beam has traversed through the plasma but before trajectory crossing occurs. As we will show later, typically the root mean square (rms) of the density modulation magnitude can reach $\Delta n/n_0 \sim 0.5$ which is large enough to be recorded. Such magnetic fields may not be strong enough to be measured using Faraday rotation effect. The rotation angle of the laser polarization due to Faraday effect is $\phi = \frac{e}{2m_e c n_c}\int n_e \boldsymbol{B}_\phi \cdot ds$, where e, m_e, c, n_c and n_e are the electron charge, electron mass, speed of light in vacuum, critical density and plasma density, respectively. If we assume both $\boldsymbol{B}_\phi$ and the plasma density are uniform then $\phi = \frac{e}{2m_e c}\frac{n_e}{n_c}BL \approx 0.03\frac{n_e}{n_c}$. For $n_e \ll n_c$, the rotation angle will be too small to be measured.

Ultrashort relativistic electron beams have been successfully used to capture the electric field structure of linear plasma wakes [33, 34], which is relatively more challenging because the wake moves at the speed of light whereas the magnetic fields associated with thermal Weibel instability are quasi-static. In this section, we show simulation results to illustrate the concept of probing magnetic fields in OFI plasmas using ultrashort relativistic electron beams. To mimic the bounded OFI plasma, the uniform plasma in previous simulations is replaced by a plasma column with a diameter of 20 c/ω_p, which corresponds to 48 μm for $n_e = 5 \times 10^{18}$ cm^{-3}. All other parameters remain unchanged. Figure 3(a) shows the self-generated magnetic fields in this bounded plasma. Each row in figure 3(a) is a y–z slice of the B_y field through the $x = 0$ plane. It can be clearly seen that the magnetic fields start to grow from random noise and resemble a quasi-static structure in a few ps. At the beginning, the spectrum of the unstable mode is the broadest, $0 < \frac{k_z c}{\omega_p} < \sqrt{A}$. Thereafter, the evolution of the magnetic fields is dominated by the most unstable mode. After $\sim$2 ps, the magnetic field structure becomes quasi-static. Figure 3(b) shows the 3D isosurface plot of the B_y field at $t = 5$ ps.

If we send an electron probe through the plasma along the $+x$ direction, the electrons will be deflected predominantly by the B_y fields since $B_z \lll B_y$. After propagating for a certain distance, the deflection will lead to density modulations which may be recorded by projecting the electron beam onto a screen that converts charge density distribution to optical intensity distribution. The modulated density profiles of the electron beam on a plane 2 mm after the plasma are shown in figure 3(c), each row corresponds to the time shown in figure 3(a). The choice of this distance will be explained later. The electron probe beam is assumed to having a uniform density (within the $\sim$300 μm field of view) therefore the density modulation will be zero if there is no plasma. We note that the snapshots shown in figure 3(c) have been convolved with a 2D Gaussian distribution with $\sigma_r = 2$ μm to account for the resolving power of the imaging system including an scintillator screen (e.g. a thin YAG:Ce crystal) which converts the electron density profile to optical signals and the following image relay optics as well as the image recording system [33]. The recorded snapshots of the electron beam reflect the structure of the magnetic fields very well, therefore from which we can infer the k-spectrum (wave-vector spectrum) of the magnetic fields directly. The results confirm the kinetic theory prediction that the thermal Weibel instability initially has a broad k spectrum (the magnetic fields have many different wavelengths) but the magnetic fields rapidly self-organize to a quasi-static structure (the magnetic fields have a predominant wavelength corresponding to the most unstable k) [15]. It can also be seen from the results that the magnitude of the density modulation of the probe beam increases with time, which is a direct reflection of growth of the magnetic fields. In figure 3(d) we show the evolution of the rms density modulation magnitude of the probe beam (the solid red line for $\varepsilon_n = 0$ and the dashed red line for $\varepsilon_n = 10$ μm, ε_n is the emittance of the electron beam) which closely follows the growth of the magnetic fields represented by the blue curve. From the red line, we can infer the linear growth rate of the thermal Weibel instability, $\gamma \approx 0.011\omega_p$. This is smaller compared with the kinetic theory prediction of $\gamma_{theory} \approx 0.018\omega_p$. This discrepancy is due to the numerical (artificial) collisions in the simulation which can be eliminated by increasing the number of particles per cell. We have confirmed this using 2D simulations with number of particles per cell larger than 1000 (which is impractical in 3D simulations due to our limited computation resources). Therefore, we extrapolate that by increasing the number of particles per cell in 3D simulations to suppress the numerical collisions the discrepancy between γ and γ_{theo} will be eliminated. Kinetic theory predicts that the collisional effect may not be negligible for high densities and will reduce the growth rate of

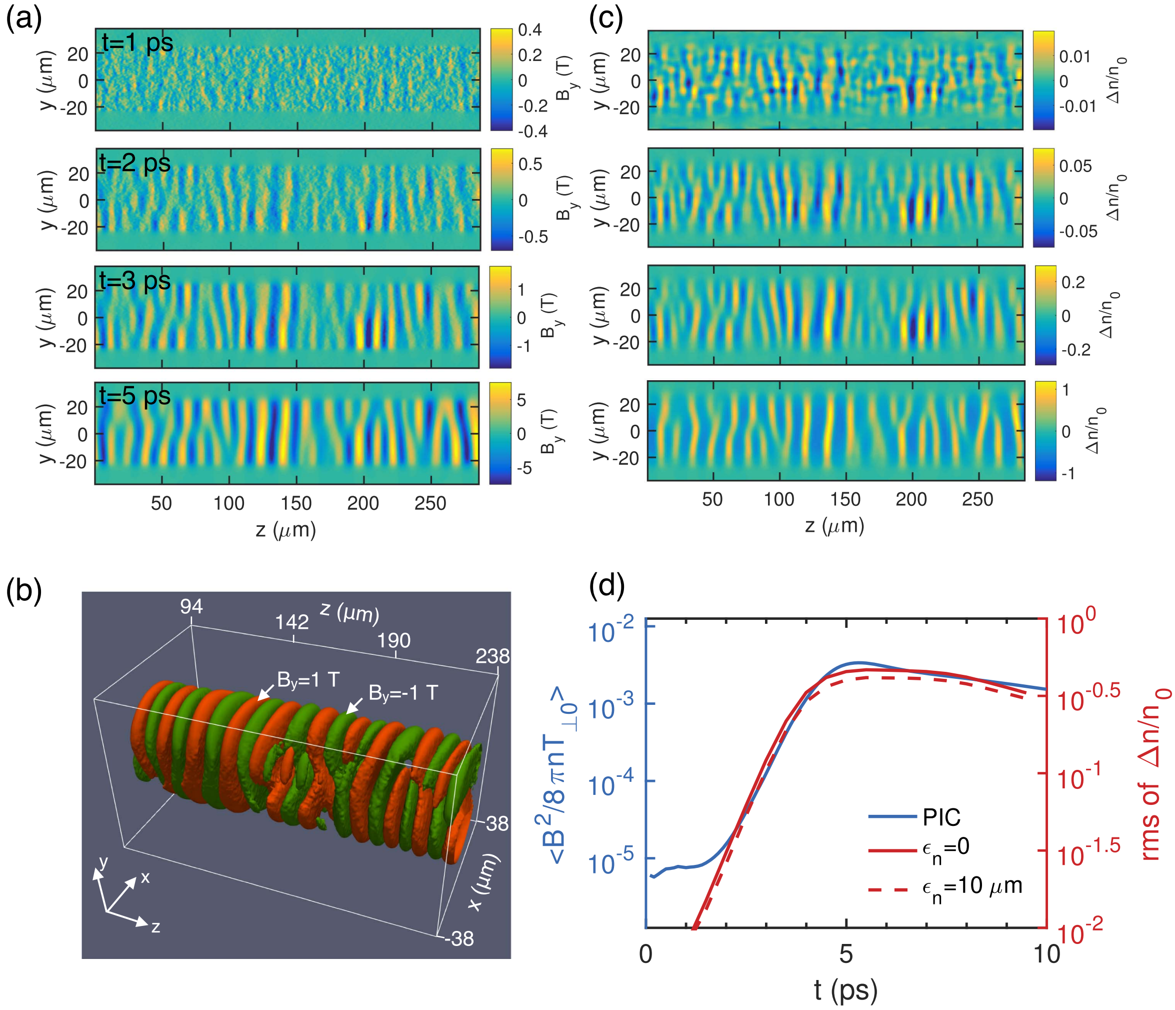

Figure 3. Probing magnetic fields driven by thermal Weibel instability using ultrashort electron beams. (a) Each row shows a slice (through $x = 0$) of the magnetic field growing in an anisotropic plasma at a different time. (b) shows the 3D isosurface plot of B_y field at 5 ps. (c) The snapshots of magnetic fields taken by a 30 MeV electron beam with a drift distance of 2 mm (see text). Each row in (a) and (c) is taken at the same time. (d) The normalized average magnetic field energy (blue line) and rms density modulation magnitude of the probe beam (red lines) as functions of time.

filamentation/Weibel instability [12, 35]. This can be potentially verified in experiment by changing plasma densities and measuring the growth rate of the instability using the method proposed here.

In figure 3(c), the snapshots are taken 2 mm behind the plasma to avoid trajectory crossing of electrons originate from different transverse portions of the beam. For a given deflection angle, the transverse displacement of an electron δ is proportional to the drift distance L, namely, $\delta = \theta L$, where θ is the deflection angle due to the magnetic field. Consequently, for small L, the density modulation $\Delta n/n_0$ is proportional to drift distance. In figure 4(a), we show snapshots of the probe beam at different drift distances from 1 mm to 10 mm. The results clearly show that for a drift distance roughly shorter than 2 mm, the density modulation of the probe beam has similar structures as that of the magnetic fields and the magnitude of the density modulation increases almost linearly as the drift distance. For larger L, trajectories of electrons from different transverse locations cross through each other so that now the density modulation of the probe beam deviates from the magnetic field structure and forms fake structures in the snapshot. The rms magnitude of the density modulation as a function of drift distance is shown in figure 4(b). It is clear that for $L < 2$ mm $\Delta n/n_0$ increases almost linearly as L, whereas for larger L, $\Delta n/n_0$ saturates. Strictly speaking, there will always be trajectory crossing for even small L. Therefore, to capture simultaneously the structure and the strength of the magnetic fields the drift distance should be limited to an optimal value for which $\Delta n/n_0$ is maximized within the region where $\Delta n/n_0$ is still a quasi-linear function of L to avoid severe trajectory crossing. This optimal drift distance L_{opt} is proportional to the energy of the probe beam therefore can be increased by using more energetic electron beams.

The effects of finite energy spread and emittance of a realistic electron beam on the results presented in previous sections are addressed here. For a fixed energy of the probe beam and a given drift distance, the predominant effect of energy spread and emittance is the change of $\Delta n/n_0$. To quantify this, we add energy spread and emittance to the

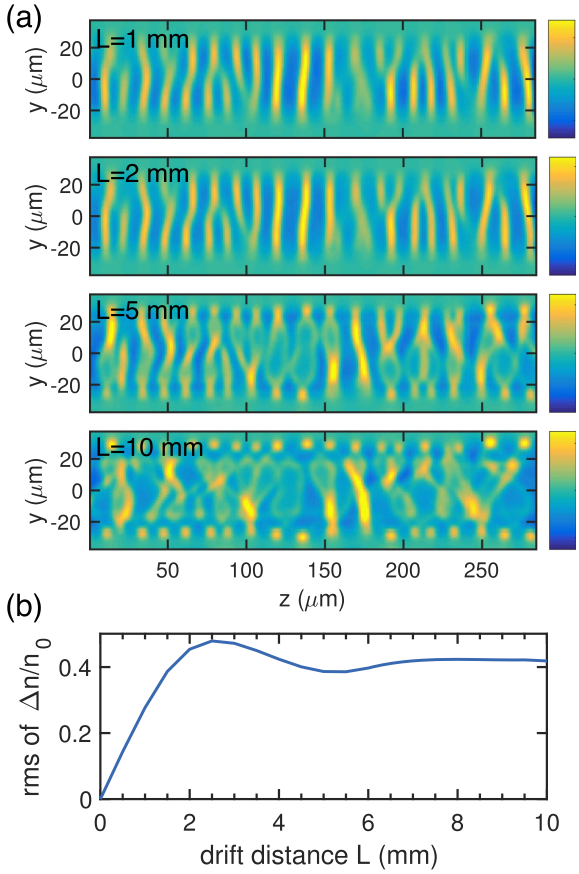

Figure 4. Density profile modulation of the 30 MeV probe beam at different drift distances. (a) Snapshots of the magnetic fields at $t = 5$ ps taken by the same electron probe beam but at four drift distances. (b) Magnitude of the density modulation as a function of drift distance.

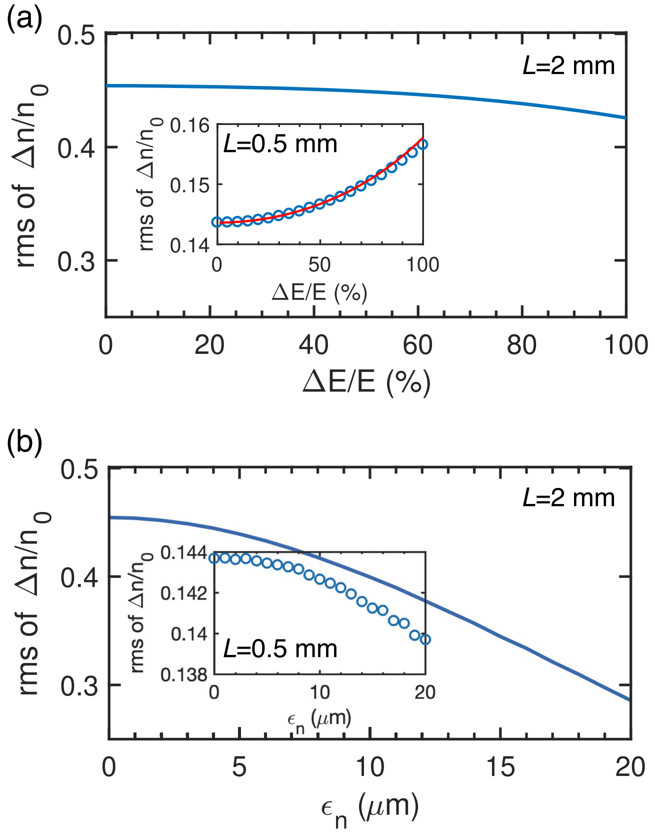

Figure 5. Magnitude of density modulation of the probe beam as functions of energy spread (a) and emittance (b). The main plots show the results taken at a drift distance of $L = 2$ mm where $\Delta n/n_0$ is maximized and the insets show the results take at $L = 0.5$ mm where the trajectory crossing effect is negligible.

probe beam in simulations and the results are shown in figure 5. The effect of the energy spread on the measured density modulation $\Delta n/n_0$ depends on the drift distance. For small drift distance where trajectory crossing is negligible, $\frac{\Delta n}{n_0} = -\nabla \cdot \vec{\delta} \propto \frac{1}{p}$, here $\vec{\delta}$ is the transverse displacement of the electron that being deflected by the magnetic fields and p is the momentum of the electron. A finite energy spread causes $\Delta n/n_0$ to increase since $\frac{1}{p_0 + \Delta p/2} + \frac{1}{p_0 - \Delta p/2} = \frac{2}{p_0}\frac{1}{1-\left(\frac{\Delta p}{2p_0}\right)^2} > 2/p_0$. Here p_0. is the mean value of the momentum and $0 < \Delta p/2 < p_0$ represents the energy spread. More generally, if the electron beam has a flattop energy spread, then $\frac{\Delta n/n_0}{(\Delta n/n_0)_0} = x^{-1}\ln\frac{2+x}{2-x}$ where $(\Delta n/n_0)_0$ is the density modulation magnitude for an ideal beam without energy spread and $x = \Delta p/p_0$ is energy spread of the beam (full width at half maximum) [36]. This is shown in the inset of figure 5(a) where the red line shows the theory and the blue circles are simulation results. For larger drift distance, the density modulation $\Delta n/n_0$ does no longer increase linearly with $1/p$ due to more trajectory crossing therefore it may drop as the ener spread of the beam increases as shown in figure 5(a) for the $L = 2$ mm case. Nevertheless, in both cases, the change of $\Delta n/n_0$ is negligible ($\lesssim$1%) as long as the energy spread is small ($\lesssim$50%). A finite emittance of the beam tends to reduce $\Delta n/n_0$ for any arbitrary drift distance as shown in figure 5(b) and as explained in [36]. However, the drop of $\Delta n/n_0$ is also negligible if the emittance of the electron beam is kept $\lesssim 5$ μm. These requirements on energy spread and emittance can be met readily by using either conventional linacs or plasma-based accelerators.

In figure 6 we show the results for the LP case. All the simulation parameters are the same as in the CP case shown in figure 3 except that the initial temperature of the plasma is set to $T_x = 150$ eV and $T_{y,z} = 10$ eV to mimic the distribution initialized by a linearly polarized laser (see figure 1(f)). As we have explained in previous sections, the topology of the magnetic fields changes due to the different temperature tensor. Therefore, the B_y and B_x fields do not have similar structures in the LP case as in the CP case. The 3D isosurface plots of B_y and B_x fields are shown in figures 6(a) and (b), respectively. The projections along two transverse directions are also shown. We point out that because now the plasma is bounded, the magnetic field structure may have changed compared to the case shown in figure 2 where the plasma is infinite large (due to the use of periodic boundary conditions). Note that the projections of the magnetic fields on the x–z plane clearly show different structures of B_y and B_x fields. It is possible to use the method we proposed to distinguish this difference. Figures 6(c) and (d) show snapshots of the B_y and

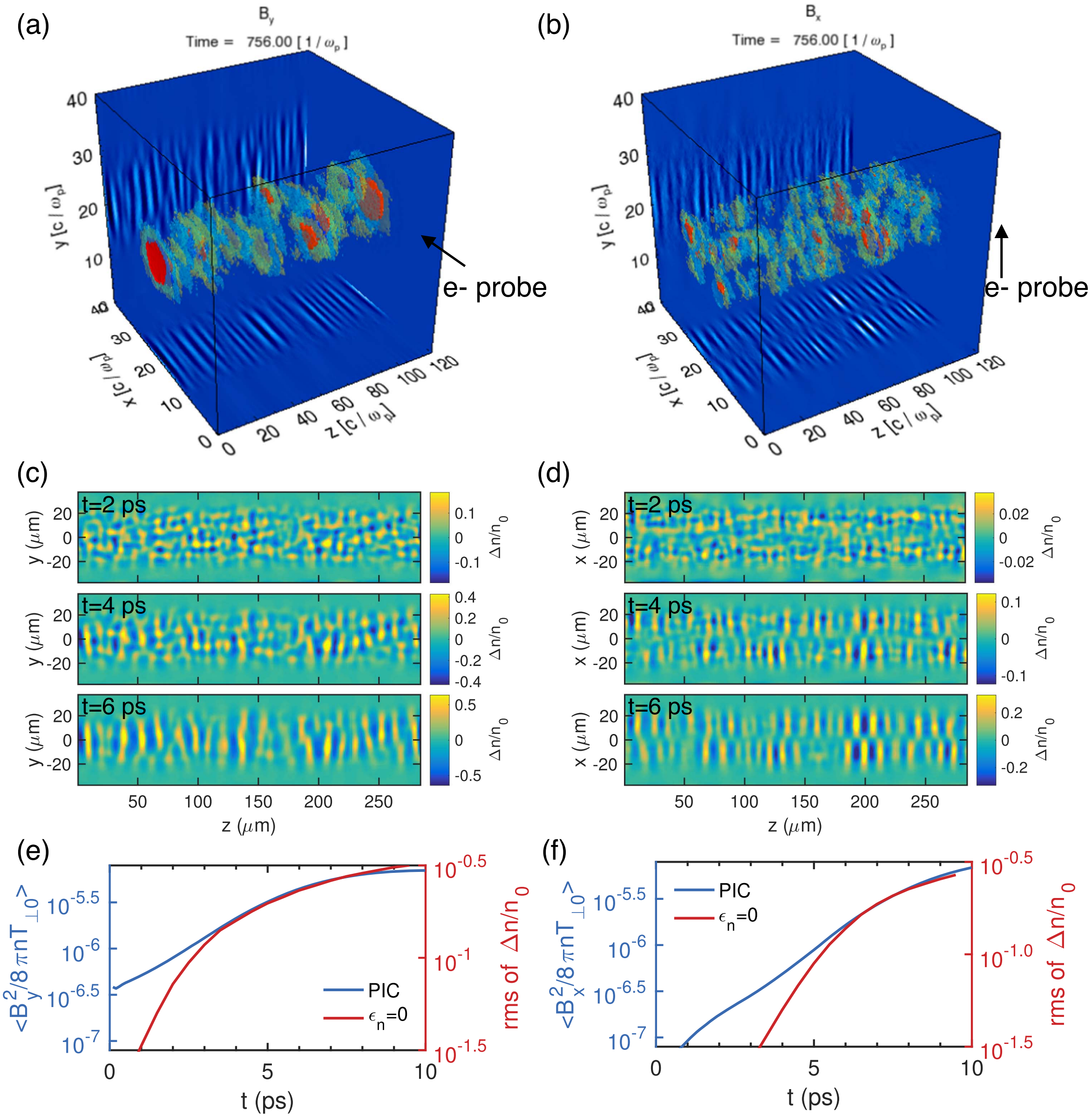

Figure 6. Magnetic fields structure and snapshots of LP case. (a) and (b) show the 3D isosurface plot and projections of the magnetic fields B_y and B_x, respectively. Note the different topological structures of the magnetic fields visible in the projections to the x–z plane. These plots are taken at $t = 6$ ps. (c) and (d) show snapshots of the B_y and B_x fields taken by the electron probe beam at different time. These snapshots are obtained by sending the electron beam through the plasma along x and y directions, respectively, as indicated by the arrows in (a) and (b). (e) and (f) show the normalized magnetic field energy (blue line) and rms density modulation magnitude of the probe beam (red lines) as functions of time correspond to (c) and (d), respectively.

B_x fields taken by the 30 MeV electron probe beam at different times. These snapshots are obtained by sending the electron beam through the plasma along x and y direction, respectively, as indicated by the arrows in (a) and (b). The drift distance is 20 mm, which is longer than that in the CP case because of the weaker magnetic fields. The different structure of B_y and B_x fields are captured by the electron probe as can be seen in figures 6(c) and (d). Also note that the magnitudes of the density modulation of the probe beam corresponding to the B_y fields are larger, indicating that $B_y \gg B_x$ which is consistent with the explanation given in previous sections. The corresponding normalized magnetic field energy (blue line) and rms density modulation magnitude of the probe beam (red lines) as functions of time are shown in figures 6(e) and (f). Once again, the density modulation magnitude of the electron probe beam tracks the magnetic field energy fairly well as soon as the magnetic fields has grown to a detectable level by this method. The deviation between the blue line and the red line for $t < 3$ ps is likely due to the overlapping of filaments. Namely, at early time the spacing between filaments is small and along the path of the electron probe beam there are multiple filaments therefore the defection contributed by these filaments may cancel out so as to reduce the modulation magnitude of the probe beam.

4. Discussion

As the pump laser ionizes neutral gas to initialize plasmas with anisotropic distributions, it also drives a wake in the plasma. The amplitude of the wake can be reduced by lowering the laser intensity. The effects of electric fields in the wake on the traversing probe beam can be further suppressed or eliminated by increasing the duration the probe beam interacts with the plasma. This can be done by either increasing the probe pulse length or by increasing the pump laser spot size to excite a broader wake. Because the plasma wake moves in the laser propagation direction at the speed of light, the average effect on deflecting the probe beam by the wake will drop dramatically for $k_p c\tau \gg 1$ where k_p is the wavenumber of the wake, $\tau = c^{-1}\sqrt{\sigma_\tau^2 + \sigma_W^2}$ is the traversing time of the probe, σ_τ is probe pulse length and σ_W is width of the wake. The density modulation of the probe beam contributed by the wake is reduced by a factor of $e^{-k_p^2 c^2 \tau^2} \ll 1$ compared to the case where the wakefileds are assumed to having the same amplitude but stationary [36]. Therefore, even for the case where the magnitude of the wakefields is comparable to the strength of the self-generated magnetic fields, the contribution from the wakefields is negligible if $k_p c\tau \gg 1$.

The optimal plasma density is limited by the spatial resolution of the imaging system, the temporal resolution required to resolve the linear growth phase of the instability and the condition required to suppress the contribution from the wakefields. Assume that the best achievable spatial resolution of the imaging system is σ_m, to resolve the structure of the magnetic fields requires $k_p\sigma_m \ll 1$. To temporally resolve the linear growth of the thermal Weibel instability requires $\gamma\tau < 1$ where $\gamma = \hat{\gamma}\omega_p$ is the growth rate of the instability. To suppress the contribution from the wakefields requires $c\tau k_p \gg 1$. The combination of these requirements set the limitation on plasma frequency as $\frac{1}{\tau} \ll \omega_p \ll \mathrm{Min}\left(\frac{1}{\hat{\gamma}\tau}, \frac{c}{\sigma_m}\right)$. A spatial resolution as small as 2–3 μm has been demonstrated in experiments [33], which gives $c/\sigma_m \sim (10\ \mathrm{fs})^{-1}$. For an OFI plasma, the kinetic theory predicts that $\hat{\gamma}$ is on the order of 0.01. These numbers indicate that the lower limit of k_p^{-1} (the upper limit of the plasma density) is restricted by σ_m unless $c\tau > 300\ \mu$m (long probe and/or wide plasma). For instance, if the traversing time is $\tau = 0.1$ ps, then the plasma density should be in the range of $3 \times 10^{16} \ll n_p(\mathrm{cm}^{-3}) \ll 3 \times 10^{18}$ which partially covers the density range widely used in laser-wakefield acceleration experiments.

Due to the fast-growing nature of the thermal Weibel instability, the jitter between the pump laser and the electron probe beam should be minimized. A rough estimate can be made by assuming that within the jitter time the instability does not grow over one e-folding, that is, $\tau_{jitter} < \frac{1}{\gamma} = \frac{1}{\hat{\gamma}}\omega_p^{-1}$. For the densities mentioned above, the jitter should be smaller than 1–10 ps, which can be readily achieved.

5. Conclusion

A laboratory platform suitable for quantitatively studying thermal Weibel instability is proposed. We show using self-consistent 3D PIC simulations that plasmas with anisotropic EVDs can be initialized by optical-field ionization. Such plasmas are unstable to thermal Weibel instability. The topological structures of the self-generated magnetic fields can be manipulated by changing the polarization of the ionizing laser. We also show that it is possible to measure the spatiotemporal evolution of the self-generated magnetic fields using an ultrashort relativistic electron beam as a probe. By taking a series of snapshots of the magnetic fields at different times, the wavevector spectrum evolution and the linear growth rate of thermal Weibel instability can be measured. Requirements on laser, plasma and probe electron beams are discussed. These proposed measurements open new possibilities to experimentally study the thermal Weibel instability—a lynchpin of kinetic instabilities in plasmas.

Acknowledgments

Simulations were performed on Hoffman cluster at UCLA, Edison and Cori clusters at National Energy Research Scientific Computing Centre (NERSC). This work was supported by NSF Grant No. 1734315 and DOE Grant DE-SC0010064.

ORCID iDs

Chaojie Zhang https://orcid.org/0000-0001-8035-3014
Chen-Kang Huang https://orcid.org/0000-0002-4478-0542

References

Q1

[1] Weibel E S 1959 Spontaneously growing transverse waves in a plasma due to an anisotropic velocity distribution *Phys. Rev. Lett.* **2** 83–4

[2] Kuramitsu Y *et al* 2011 Time evolution of collisionless shock in counterstreaming laser-produced plasmas *Phys. Rev. Lett.* **106** 175002

[3] Fiuza F, Fonseca R A, Tonge J, Mori W B and Silva L O 2012 Weibel-instability-mediated collisionless shocks in the laboratory with ultraintense lasers *Phys. Rev. Lett.* **108** 235004

[4] Huntington C M *et al* 2015 Observation of magnetic field generation via the Weibel instability in interpenetrating plasma flows *Nat. Phys.* **11** 173–6

[5] Matsumoto Y, Amano T, Kato T N and Hoshino M 2015 Stochastic electron acceleration during spontaneous turbulent reconnection in a strong shock wave *Science* **347** 974–8

[6] Benedetti A, Tamburini M and Keitel C H 2018 Giant collimated gamma-ray flashes *Nat. Photon.* **12** 319–23

[7] Medvedev M V and Loeb A 1999 Generation of magnetic fields in the relativistic Shock of gamma-ray burst sources *Astrophys. J.* **526** 697–706

[8] Widrow L M, Ryu D, Schleicher D R G, Subramanian K, Tsagas C G and Treumann R A 2012 The first magnetic fields *Space Sci. Rev.* **166** 37–70

[9] Ryu D, Schleicher D R G, Treumann R A, Tsagas C G and Widrow L M 2012 Magnetic fields in the large-scale structure of the universe *Space Sci. Rev.* **166** 1–35

[10] Gregori G *et al* 2012 Generation of scaled protogalactic seed magnetic fields in laser-produced shock waves *Nature* **481** 480–3

[11] Fried B D 1959 Mechanism for instability of transverse plasma waves *Phys. Fluids* **2** 337

[12] Bret A, Gremillet L and Dieckmann M E 2010 Multidimensional electron beam-plasma instabilities in the relativistic regime *Phys. Plasmas* **17** 120501

[13] Tzoufras M, Ren C, Tsung F S, Tonge J W, Mori W B, Fiore M, Fonseca R A and Silva L O 2006 Space-charge effects in the current-filamentation or weibel instability *Phys. Rev. Lett.* **96** 105002

[14] Bret A, Gremillet L and Bellido J C 2007 How really transverse is the filamentation instability? *Phys. Plasmas* **14** 032103

[15] Romanov D V, Bychenkov V Y, Rozmus W, Capjack C E and Fedosejevs R 2004 Self-organization of a plasma due to 3D Evolution of the weibel instability *Phys. Rev. Lett.* **93** 215004

[16] Tatarakis M *et al* 2003 Propagation instabilities of high-intensity laser-produced electron beams *Phys. Rev. Lett.* **90** 175001

[17] Mondal S *et al* 2012 Direct observation of turbulent magnetic fields in hot, dense laser produced plasmas *Proc. Natl Acad. Sci.* **109** 8011–5

[18] Jung R *et al* 2005 Study of electron-beam propagation through preionized dense foam plasmas *Phys. Rev. Lett.* **94** 195001

[19] Allen B, Yakimenko V, Babzien M, Fedurin M, Kusche K and Muggli P 2012 Experimental study of current filamentation instability *Phys. Rev. Lett.* **109** 185007

[20] Manclossi M, Santos J J, Batani D, Faure J, Debayle A, Tikhonchuk V T and Malka V 2006 Study of ultraintense laser-produced fast-electron propagation and filamentation in insulator and metal foil targets by optical emission diagnostics *Phys. Rev. Lett.* **96** 125002

[21] Huntington C M *et al* 2011 Current filamentation instability in laser wakefield accelerators *Phys. Rev. Lett.* **106** 105001

[22] Fox W, Fiksel G, Bhattacharjee A, Chang P-Y, Germaschewski K, Hu S X and Nilson P M 2013 Filamentation instability of counterstreaming laser-driven plasmas *Phys. Rev. Lett.* **111** 225002

[23] Park H-S *et al* 2015 Collisionless shock experiments with lasers and observation of Weibel instabilities *Phys. Plasmas* **22** 056311

[24] Zhou S, Bai Y, Tian Y, Sun H, Cao L and Liu J 2018 Self-organized kilotesla magnetic-tube array in an expanding spherical plasma irradiated by kHz femtosecond laser pulses *Phys. Rev. Lett.* **121** 255002

[25] Morse R L and Nielson C W 1971 Numerical simulation of the weibel instability in one and two dimensions *Phys. Fluids* **14** 830

[26] Yoon P H and Davidson R C 1987 Exact analytical model of the classical Weibel instability in a relativistic anisotropic plasma *Phys. Rev.* A **35** 2718–21

[27] Kalman G 1968 Anisotropic temperature plasma instabilities *Phys. Fluids* **11** 1797

[28] Fonseca R A *et al* 2002 OSIRIS: a three-dimensional, fully relativistic particle in cell code for modeling plasma based accelerators *Computational Science — ICCS 2002* ed P M A Sloot *et al* (Berlin: Springer) pp 342–51

[29] Ammosov M V, Delone N B and Krainov V P 1986 Tunnel ionization of complex atoms and atomic ions in electromagnetic field *Sov. Phys.—JETP* **64** 138

[30] Huang C K, Zhang C J, Marsh K A, Clayton C E and Joshi C 2019 Initializing anisotropic and unstable electron velocity distributions needed for investigating plasma kinetic instabilities *Plasma Phys. Control. Fusion* unpublished Q2

[31] Zhang C, Huang C-K, Marsh K A, Clayton C E, Mori W B and Joshi C 2019 Ultrafast optical field–ionized gases—a laboratory platform for studying kinetic plasma instabilities *Sci. Adv.* **5** eaax4545

[32] Buck A, Nicolai M, Schmid K, Sears C M S, Sävert A, Mikhailova J M, Krausz F, Kaluza M C and Veisz L 2011 Real-time observation of laser-driven electron acceleration *Nat. Phys.* **7** 543–8

[33] Zhang C J *et al* 2017 Femtosecond probing of plasma wakefields and observation of the plasma wake reversal using a relativistic electron bunch *Phys. Rev. Lett.* **119** 064801

[34] Zhang C J *et al* 2018 Probing plasma wakefields using electron bunches generated from a laser wakefield accelerator *Plasma Phys. Control. Fusion* **60** 044013

[35] Hao B, Sheng Z-M and Zhang J 2008 Kinetic theory on the current-filamentation instability in collisional plasmas *Phys. Plasmas* **15** 082112

[36] Zhang C J *et al* 2016 Capturing relativistic wakefield structures in plasmas using ultrashort high-energy electrons as a probe *Sci. Rep.* **6** 29485